Identification of antinodes and zero-surface-strain contours of flexural vibration with time-averaged speckle pattern shearing interferometry

W. O. Wong, K. T. Chan, and T. P. Leung

A new time-averaged frame subtraction technique is introduced for vibration analysis by digital speckle shearing interferometry. The technique permits the enhancement of fringes by subtracting two Bessel fringe patterns at different forcing levels. Compared with the phase-shift method, this method is more efficient and easier to implement for qualitative vibration measurement, providing a means for fast inspection of plate vibration behavior. It is also capable of tracing contours of zero strain and locating antinodes on vibrating plates. © 1997 Optical Society of America

Key words: Time-averaged speckle pattern shearing interferometry, digital shearography, vibration mode shape, antinodes, zero-strain distribution.

1. Introduction

In vibration and acoustics, a knowledge of modal frequency and shape of vibration is important for gaining insight into the vibration behavior of structures. In mathematical terms, these two characteristics are related to the eigenvalues and eigenfunctions of the system. In a general bending vibration problem, however, they are not readily available, as the closed-form solutions to the fourth-order differential equation may not exist.[1] Mode shapes and frequencies are therefore required to be measured experimentally. Traditional methods use accelerometers and signal analyzers for modal analysis. Although they are precise and reliable for measuring modal parameters for structural modeling, the methods are pointwise, time consuming, and contacting. Optical vibrometers are the modern alternative to accelerometers. They are noncontacting. However, they are still a pointwise instrument and would be time consuming for modal analysis.

Holographic interferometry has been a well-known noncontacting technique for vibration measurement in the full field. It has been deterred by dark-room film-development practice from wide applications. However, the principle has been employed to develop a dry type of interferometry, known as electronic speckle pattern interferometry (ESPI). The further development of the basic technique has led to a more convenient setup, shearography, which measures the vibration amplitude gradient directly.[2,3] The electronic version of this is often referred to as electronic speckle shearing interferometry. The capability of ESPI or shearography has now been enhanced by the use of high-speed computers with modern image processors.[3–5] The phase-shift method has permitted both techniques for analyzing vibration quantitatively.[6]

ESPI-based methods of measuring vibration have a few different techniques, for example, the time-averaged technique, the stroboscopic technique, and the pulsed laser technique. This paper concerns the time-averaged technique only. In the traditional time-averaged ESPI technique, after dc filtering and rectification, the monitored fringe pattern is the squared zero-order Bessel function of the vibration amplitude with a very low high-order fringe contrast. Only a few orders can be visualized directly from the screen, making the quantitative measurement of vibration difficult if not impossible. The sinusoidal phase-modulation technique[2] permits a complete mapping of the amplitude and the phase contours

across any vibrating surface. In this technique, one of the light paths is modulated with a sinusoidal frequency equal to the frequency of and in synchronization with the vibration of the structure. This permits the time-averaged ESPI to measure the phase of vibration.[7]

Comparing ESPI and shearography, one would sometimes favor shearography. This is because ESPI is influenced by vibration and the temperature of the environment, whereas shearography is relatively insensitive to rigid body motion and environmental factors. Moreover, when higher-order derivatives of vibration amplitude are measured, shearography is more suitable than ESPI.[8]

Nakadate *et al.*[3] have used a frame subtraction method in speckle shearing interferometry to measure the vibration amplitude gradient, showing better fringe contrast but less measurement sensitivity than that of single-image time-averaged shearography. In the regions of high vibration gradients, the presence of nonzero minimal points of the fringe function would limit the fringe visibility. For a given background noise level, the nonzero minima are responsible for the deterioration of the fringe contrast.[9] Nakadate[10] and Saldner *et al.*[6] have employed the phase-step method, trying to measure plate vibration mode shapes quantitatively. By this method, they obtained better fringe visibility and quantitative vibration values on the plates. The method they used requires one to grab several frames of images for one measurement and to process the image data point by point. Recent advancements in computer and image-processing technologies may help to improve the speed. Nevertheless, for certain vibration analyses, a quantitative measurement might not be necessary. In such a situation, fringe visibility and measurement efficiency are relatively more important.

In this paper, a new time-averaged frame subtraction technique is introduced for vibration analysis by digital speckle shearing interferometry. The experimental setup is similar to the traditional shearographic measurement system, but the technique permits the enhancement of fringes by the subtraction of two Bessel fringe patterns at different forcing levels. As far as the qualitative measurement of vibration is concerned, the present technique is more efficient and easier than the phase-shift method for fringe enhancement. Furthermore, the new technique provides a means for the fast inspection of the vibration behavior of a structure. A fringe interpretation method is also described for the convenient identification of antinodal positions and contours of zero strains of plate vibration.

2. Theory of Measurement

Transverse vibration is measured by using the time-averaged shearing interferometry method. The schematic diagram of the optical setup is shown in Fig. 1. The object is either a cantilever beam or a clamped circular plate, each with a diffuse surface. Vibration is assumed to be linear in this study. Pho-
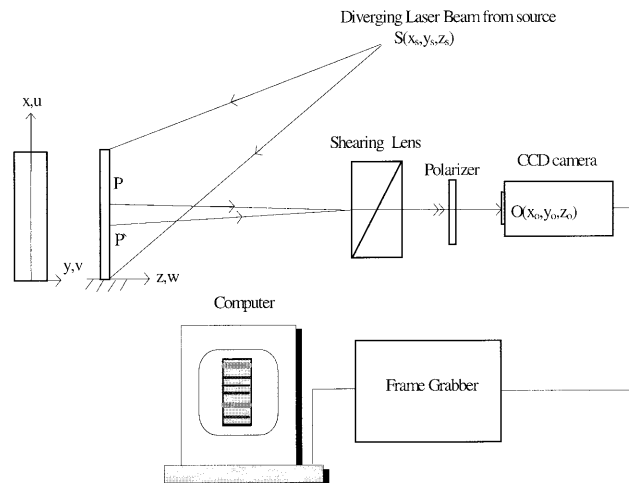

Fig. 1. Schematic setup of time-average speckle pattern shearing interferometry.

tographic films will not be used. Instead a CCD imaging system is used with a shearing lens of the birefringent type. A suitable polarizer is employed to bring the two emerged orthogonally polarized wave fronts to the same polarization to ensure the best interference. The framegrabber is controlled by a microcomputer for image processing. A He–Ne laser is used as a light source. Its wavelength is λ.

The shearing lens brings the rays from two points P and P′ on the object surface to a point O in the CCD camera. The shearing lens is made and oriented to let points P and P′ be represented by coordinates (x, y, z) and $(x + \delta x, y, z)$, respectively. That is, the image of the object is sheared in the x axis; δx should be small enough to obtain a sufficient accuracy of the gradient measurement and a good interference of the light beams. The intensity of the image recorded by the camera is written as[11]

$$I_s = 2 I_o(1 + \cos \phi), \qquad (1)$$

where I_o is the object image intensity at O and ϕ is the phase difference between light paths from P′ and P to O. Here I_o and ϕ are random in space over the image surface.
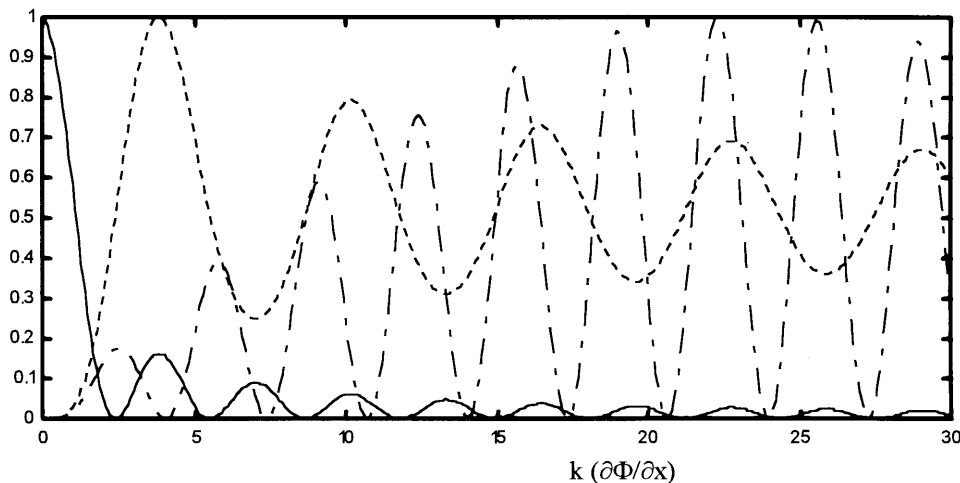
Consider vibration at the nth natural mode of frequency ω_n. The out-of-plane displacement of the object is expressed as

$$w(x, y, t) = w_o(x, y)\cos \omega_n t, \qquad (2)$$

where $w_o(x, y)$ is the vibration amplitude at (x, y), representing a standing wave at frequency ω_n.

The vibrations of P and P′ are, in general, represented by (u, v, w) and $(u + \delta u, v + \delta v, w + \delta w)$, respectively. These produce a further phase shift between the light paths to point O in the image plane. Equation (1) then becomes

$$I = 2I_o[1 + \cos(\phi + \Delta)], \qquad (3)$$

- - - - - $[1-J_o(k\,(\partial\Phi/\partial x)]^2$
— - — $\{J_o[r_1\,k\,(\partial\Phi/\partial x)] - J_o[r_2\,k\,(\partial\Phi/\partial x)]\}^2$, $r_1 = 1$, $r_2 = 0.8$
——— $J_o^2[k\,(\partial\Phi/\partial x)]$

Fig. 2. Comparison of different Bessel fringe functions (normalized values).

where

$$\Delta = \frac{2\pi}{\lambda}(A\delta x + A\delta u + B\delta v + C\delta w), \qquad (4)$$

$$A = \frac{x - x_o}{R_o} + \frac{x - x_s}{R_s},$$

$$B = \frac{y - y_o}{R_o} + \frac{y - y_s}{R_s},$$

$$C = \frac{z - z_o}{R_o} + \frac{z - z_s}{R_s}, \qquad (5)$$

$R_o^{\,2} = x_o^{\,2} + y_o^{\,2} + z_o^{\,2}$, and $R_s^{\,2} = x_s^{\,2} + y_s^{\,2} + z_s^{\,2}$. According to Hung,[12] A, B, and C are sensitivity factors relating to the illumination position point $S(x_s, y_s, z_s)$ and the camera image point $O(x_o, y_o, z_o)$.

Because δx is small, Eq. (4) can be rewritten as

$$\Delta = \frac{2\pi}{\lambda}\left(A + A\frac{\partial u}{\partial x} + B\frac{\partial v}{\partial x} + C\frac{\partial w}{\partial x}\right)\delta x. \qquad (6)$$

With normal illumination and normal viewing $x_s = y_s = x_o = y_o = 0$, and for R_o and R_s to be large compared with the object dimensions, $A \cong 0$, $B \cong 0$, and $C \cong 2$. Then, by substitution of Eq. (2) into Eq. (6),

$$\Delta = \frac{4\pi}{\lambda}(\delta x)\frac{\partial w}{\partial x} = \frac{4\pi}{\lambda}(\delta x)\frac{\partial w_o}{\partial x}\cos(\omega_n t). \qquad (7)$$

For ω_n very much higher than the grabbing rate of the imaging system, the intensity distribution recorded by the CCD camera will be the average intensity value expressed by

$$I_{avg} = \frac{1}{T}\int_0^T 2I_o\Big[(1 + \cos(\phi + \Delta)]\mathrm{d}t$$

$$= \frac{1}{T}\int_0^T 2I_o\left\{1 + \cos\left[\phi + \frac{4\pi}{\lambda}(\partial x)\frac{\partial w_o}{\partial w}\cos(\omega_n t)\right]\right\}\mathrm{d}t$$

$$= 2I_o\left\{1 + \cos\phi\,J_o\left[\frac{4\pi}{\lambda}(\delta x)\frac{\partial w_o}{\partial x}\cos(\omega_n t)\right]\right\}, \qquad (8)$$

where J_o is the Bessel function of the first kind of the zeroth order and T is the grabbing time of one image record.

Subtracting Eq. (1) from Eq. (8), one obtains

$$\Delta I = I_s - I_{avg}$$

$$= 2I_o\cos\phi\left\{1 - J_o\left[\frac{4\pi}{\lambda}(\delta x)\frac{\partial w_o(x,y)}{\partial x}\right]\right\}. \qquad (9)$$

To evaluate the average brightness of the fringe on the TV monitor, one may assume that the resultant light amplitude at the CCD obeys zero-mean circular complex Gaussian statistics.[13] The assumption is justified as the object in this study has a diffuse surface. According to Nakadate et al.,[3] if the signal after subtraction is square-law detected, the average brightness of the fringe is proportional to

$$E(x,y) = c\left\{1 - J_o\left[k\,\frac{\partial w_o(x,y)}{\partial x^2},\right.\right. \qquad (10)$$

where $c = (\langle I_s\rangle^2\,T^2/2)$ and $k = 4\pi(\delta x/\lambda)$. In time-averaged ESPI, the vibration analyzed is usually a normal mode. Therefore, $w_o(x,y)$ in Eq. (10) is the mode shape written as $r\Phi_n(x,y)$, with r depending on the magnitude of the force excitation. Here $\Phi_n(x,y)$ is referred to as the normalized mode shape; c is a

function of x and y. For a specified x and y, c is a constant with a value depending on the optical image setup and the grabbing time.

Equation (10) and Fig. 2 show that the method of Ref. 3 has a disadvantage. It is because the fringe visibility described by the Bessel function is decreasing at higher-order loops because of the presence of nonzero minima of the fringe function. From Eq. (8) and the same figure, the traditional single-frame J_o^2 fringe pattern also has low visibility at higher-order loops. This is due to the presence of the self-interference term, $2I_o$, of the equation.

In view of the above, an attempt is made here to improve the Bessel fringe visibility by a new fringe-generation method. The method generates time-averaged vibration fringes by subtracting two Bessel fringe patterns at two different forcing levels. By rewriting Eq. (2) for these two levels, we see that the linear vibration displacements are

$$w_1(x, y, t) = r_1 \Phi_n(x, y) \cos \omega_n t, \qquad (11a)$$

$$w_1(x, y, t) = r_1 \Phi_n(x, y) \cos \omega_n t, \qquad (11b)$$

where r_1 and r_2 are amplitudes determined by the forcing levels used and Φ_n is the nth normalized mode shape. The brightness of the new fringe function is then proportional to

$$E(x, y) = c \left\{ J_o \left[r_1 k \frac{\partial \Phi_n(x, y)}{\partial x} \right] - J_o \left[r_2 k \frac{\partial \Phi_n(x, y)}{\partial x} \right] \right\}^2. \qquad (12)$$
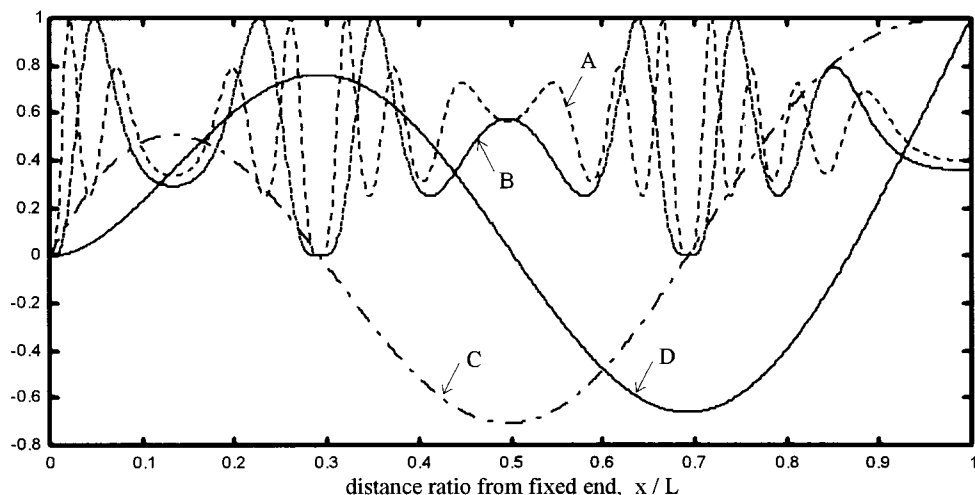
A - - - - - - - Normalized brightness of time-average Bessel fringes [Eq. (10) with k=8π]
B — — — Normalized brightness of time-average Bessel fringes [Eq. (10) with k=4π]
C — · — · relative vibration amplitude gradient of the 3rd vibration mode shape of a cantilever beam
D ———— relative vibration amplitude of the 3rd bending mode shape of a cantilever beam

(a)
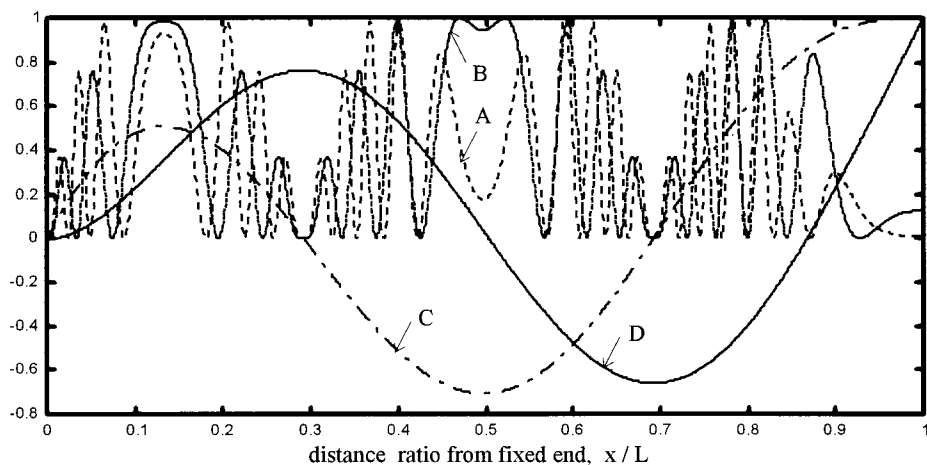
A - - - - - - Normalized brightness of time-averaged Bessel fringes [Eq.(12) with r₁=2 and r₂=1.6]
B — — — Normalized brightness of time-averaged Bessel fringes [Eq.(12) with r₁=1.5 and r₂=1.2]
C — · — relative vibration amplitude gradient of the 3rd bending mode shape of a cantilever
D ———— relative vibration amplitude of the 3rd bending mode shape of a cantilever beam

(b)

Fig. 3. Normalized brightness of time-averaged Bessel fringes with the vibration amplitude and vibration amplitude gradient of a cantilever beam, calculated with (a) Eq. (10), (b) Eq. (12).

Quite clearly, Eq. (10) can be treated as a special case of Eq. (12) when r_1 is zero. Take a cantilever beam as an example. Figure 2 shows the brightness function computed by Eq. (12). As we can see in the figure, for the higher-order loops, the visibility is markedly improved compared with the contrast of the fringes calculated by Eq. (10) or by $J_o{}^2$. Such enhancement can be obtained by adjusting the ratio between r_1 and r_2. In this case, r_1 = 1 and r_2 = 0.8. From our analysis, the result shows that electronic noise and camera noise would exert appreciable influences on the fringe contrast value. A separate paper has already been prepared to study this and will be published elsewhere.

According to the mathematical table, $J_0{}^2[k(\partial\Phi_n/\partial x)]$ is close to $[2/(\pi k \partial\Phi_n/\partial x)]\cos^2[k(\partial\Phi_n/\partial x) - (\pi/4)]$ when the argument $k(\partial\Phi_n/\partial x)$ is very large. The fringe function described by Eq. (12) has zeros at intervals approximately equal to $2\pi/(r_1 + r_2)$. Thus, not only has the fringe contrast been improved, but also the loss of sensitivity of the subtraction method of Nakadate et al.[3] has been recovered. With this enhancement of fringe pattern, the number of fringes that can be resolved by this method is increased dramatically, leading to a better spatial resolution of the vibration mode measurement.

3. Shearographic Image Pattern: Interpretation

A. Fringe Pattern Caused by Beam Vibration

As an illustration, the third bending vibration mode shape of the cantilever beam of length L and its derivative are considered first. They are calculated and plotted as curves D and C in both Figs. 3(a) and 3(b). The curves are simply for reference in the description of the features of the fringe functions, which are given below. The vertical axes are the ratios of the local vibration amplitudes or their gradients to the maximum values at the free end of the cantilever beam. Figure 3(a) is for the brightness functions calculated by Eq. (10), shown as curves A and B in the diagram for two forcing levels. Figure 3(b) is for the same functions calculated by Eq. (12), also shown as curves A and B, respectively, for two forcing levels.

We can see in Fig. 3(b) that, except for the location of contraflexure, the minimum brightness value as it occurs is zero. As mentioned above, the fringe visibility in the case of Fig. 3(b) should be much better than that of Fig. 3(a).

There are two interesting features about the fringe patterns. One, Eqs. (10) and (12) show that $(\partial\Phi_n/\partial x) = 0$ at the antinodal positions, implying that the fringes should be completely dark because $E = 0$. (For a cantilever beam, of course, the gradient at the built-in end is also zero. A dark fringe also appears there.) Two, at the points of contraflexure of the vibrating beam, the brightness values are either maxima or minima. We can see this by using the following equations derived from differentiating Eqs.

(10) and (12), respectively:

$$\frac{\partial E}{\partial x} = 2ck\left\{1 - J_o\left[k\,\frac{\partial\Phi_n(x)}{\partial x}\right]\right\}J_1\left[k\,\frac{\partial\Phi_n(x)}{\partial x}\right]\left[\frac{\partial^2\Phi_n(x)}{\partial x^2}\right],$$

$$(13)$$

$$\frac{\partial E}{\partial x} = 2ck\left\{J_o\left[r_1 k\frac{\partial\Phi_n(x)}{\partial x}\right] - J_o\left[r_2 k\frac{\partial\Phi_n(x)}{\partial x}\right]\right\}$$
$$\times \left\{r_1 J_1\left[r_1 k\frac{\partial\Phi_n(x)}{\partial x}\right] - r_2 J_1\left[r_2 k\frac{\partial\Phi_n(x)}{\partial x}\right]\right\}$$
$$\times \left[\frac{\partial^2\Phi_n(x)}{\partial x^2}\right], \tag{14}$$

where J_1 is the Bessel function of the first order. At these locations of maxima and minima, the second derivative $\partial^2\Phi_n/\partial x^2 = 0$. The surface strains induced by bending at these locations should be zero. As vibration of the beam at a natural frequency behaves as a standing wave, the locations of zero-bending strains and antinodes should be stationary. The fringes formed there should be unmoved.

As shown in Figs. 3(a) and 3(b), the zeroth-order fringes of high contrast appear at the antinodes while the high-order fringes of low contrast appear at the contraflexure locations. As we can see from the figures, in between the consecutive zero-strain and antinodal locations, we can increase the number of fringes by increasing the amplitude of the standing wave. Because $k = 4\pi(\delta x/\lambda)$ in Eqs. (10) and (12), we can conclude that we can also increase the number of fringes by increasing the shearing amount, δx, reducing the light wavelength, or both. Thus, a continuous increase of any one of these factors, e.g., vibration amplitude, will apparently generate higher-order fringes starting from the locations of contraflexure to the antinodes. Therefore, the zero-strain positions can be identified as the emanators of higher-order fringes and antinodal positions can be identified as attractors of them.

B. Fringe Pattern Caused by Flexural Plate Vibration

The first asymmetrical bending vibration mode shape of a circular plate is considered here for illustration.
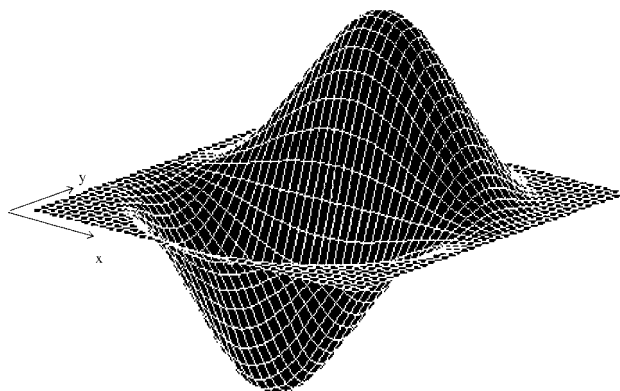

Fig. 4. First asymmetrical bending mode shape of a circular plate with a clamped boundary condition.

The equation used to calculate the mode shape shown in Fig. 4 is from Chen and Zhou.[14]   For flexural plate vibration, antinodal points occur when $\partial\Phi_n/\partial x = 0$ and $\partial\Phi_n/\partial y = 0$. Substituting the first condition into Eq. (12) gives

$$E_1(x, y) = c\left\{J_o\left[r_1 k\,\frac{\partial\Phi_n(x, y)}{\partial x}\right] - J_o\left[r_2 k\,\frac{\partial\Phi_n(x, y)}{\partial x}\right]\right\}^2$$

$$= 0. \tag{15}$$

By shearing the plate image in the y direction, a procedure similar to that in Eqs. (3)–(12) will give

$$E_2(x, y) = c\left\{J_o\left[r_1 k\,\frac{\partial\Phi_n(x, y)}{\partial y}\right] - J_o\left[r_2 k\,\frac{\partial\Phi_n(x, y)}{\partial y}\right]\right\}^2$$

$$= 0. \tag{16}$$

Equations (15) and (16) indicate that high-contrast dark-fringe curves represent the zero gradient contours in the x and y directions, respectively.   If these two fringe patterns are made to overlap properly, the intersections of these contours will give the locations of the plate vibration antinodes. These contours would be unmoved when the plate vibration is of a normal mode.

For a plate in flexure, the relationships between surface strains and deflection are given as

$$\varepsilon_x = h\,\frac{\partial^2 w}{\partial x^2},$$

$$\varepsilon_y = h\,\frac{\partial^2 w}{\partial y^2},$$

$$\gamma_{yx} = 2\,h\,\frac{\partial^2 w}{\partial y \partial x}, \tag{17}$$

where ε_x, ε_y are the flexural strains of the plate in the x and y directions, respectively; γ_{yx} is the surface shear strain; and h is half the thickness of the plate. Differentiating Eq. (15) with respect to x gives

$$\frac{\partial E_1}{\partial x} = 2ck\left\{J_o\left[r_1 k\frac{\partial\Phi_n(x)}{\partial x}\right]\right.$$

$$\left. - J_o\left[r_2 k\frac{\partial\Phi_n(x)}{\partial x}\right]\right\}\left\{r_1 J_1\left[r_1 k\frac{\partial\Phi_n(x, y)}{\partial x}\right]\right.$$

$$\left. - r_2 J_1\left[r_2 k\frac{\partial\Phi_n(x)}{\partial x}\right]\right\}\left[\frac{\partial^2\Phi_n(x, y)}{\partial x^2}\right]. \tag{18}$$

Furthermore, $\partial E_1/\partial x = 0$ gives local maxima or minima for the brightness function E_1 at the locations where the second derivatives, $\partial^2\Phi_n/\partial x^2 = 0$, form unmoved locations of contraflexural (in the x direction) points of the vibrating plate at a natural frequency. At these contraflexural locations, $\varepsilon_x = 0$. The loci tracing these contraflexural points would represent the zero-strain contours on the surface of the vibrating plate. These points can be located by finding the points on the shearographic fringe pattern, $\partial\Phi_n/\partial x$, that have tangent lines parallel to the x axis.   They are points of zero slope in
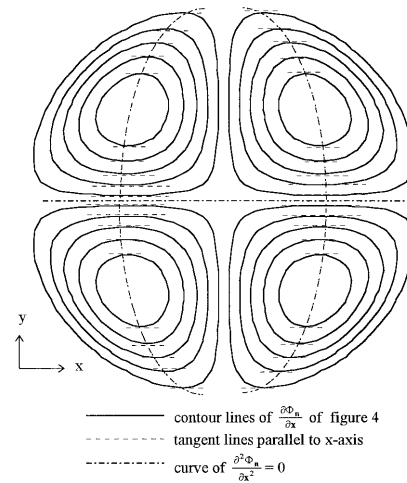

Fig. 5.   Contours of the vibration amplitude gradient and zero flexural strain of a circular plate with a clamped boundary.
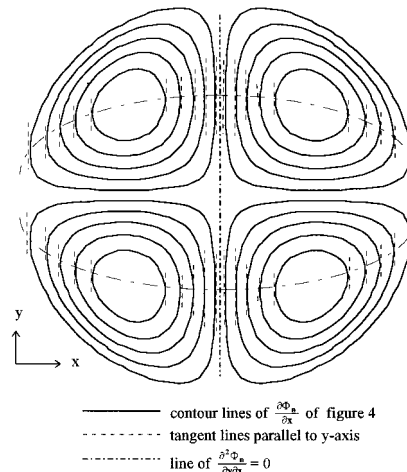

Fig. 6.   Contours of the vibration amplitude gradient and zero shear strain of a circular plate with a clamped boundary.
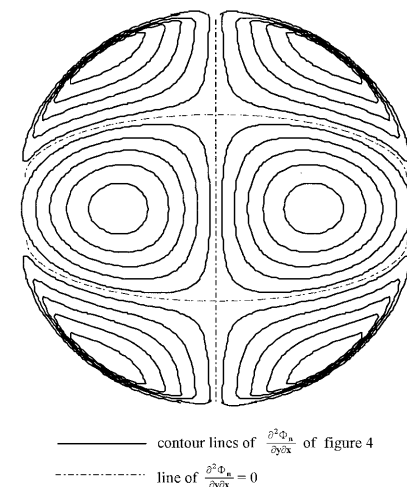

Fig. 7.   Contours of the surface shear strain of a circular plate with a clamped boundary.
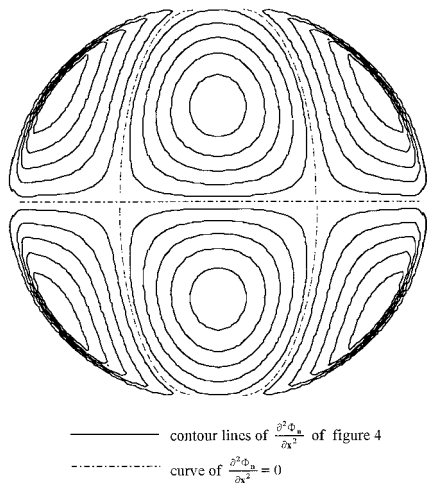
Fig. 8. Contours of the surface flexural strain of a circular plate with a clamped boundary.

the fringe pattern, as illustrated in Fig. 5. Similarly, the loci of zero shear strain, $\gamma_{yx} = 0$, can be traced by finding the points on the similar fringe pattern that have tangent lines parallel to the y axis, as shown in Fig. 6. Figures 7 and 8 give

fringe patterns, representing the contours of $\partial^2 \Phi_n / \partial y \partial x$ and $\partial^2 \Phi_n / \partial x^2$, respectively; each is computed by numerical differentiation of Fig. 4 directly. From the two figures, we can see that the contours for $\partial^2 \Phi_n / \partial y \partial x = 0$ and $\partial^2 \Phi_n / \partial x^2 = 0$ are exactly the same curves as in Figs. 6 and 5, traced by the method introduced above. By the same procedure as above, differentiating E_2 of Eq. (16) with respect to y or x will give a similar conclusion as for the contours of $\varepsilon_y = 0$ and $\gamma_{xy} = 0$.

4. Experiments

Experiments are carried out to verify the theory and to prove the observations based on the above analyses of the computed fringe patterns.

Figure 1 shows the experimental shearographic system setup. Shearograms are generated by a real-time frame subtraction method at a video rate of 30 frames/s. They can be stored in a hard disk or displayed on a monitor. Hard copies of the fringe patterns can be printed by a video printer.

Figures 9 and 10 show the shearographic results for the third bending mode of the cantilever and the first asymmetrical mode of the clamped plate, respectively. That is, $w_o = r\Phi_n$, $n = 3$ for the beam, or $n = 2$ for the
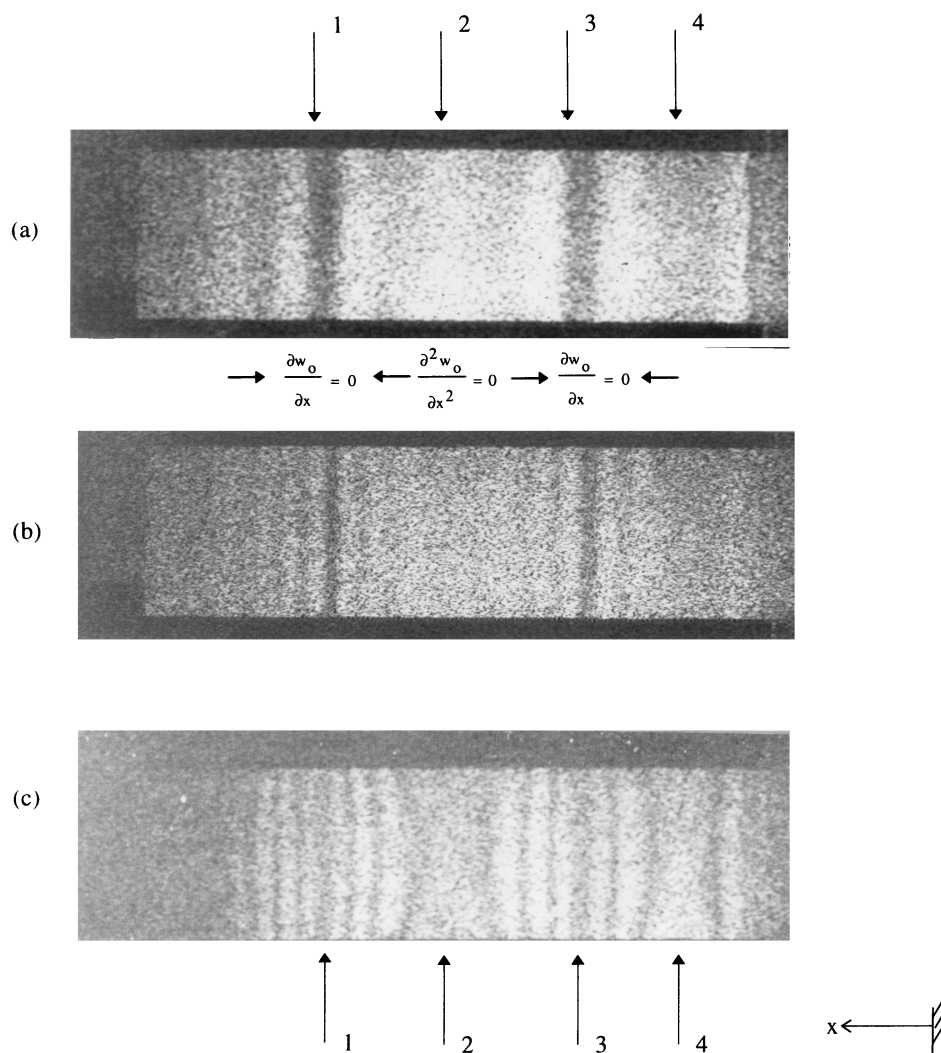

Fig. 9. Time-averaged fringes of a cantilever beam vibrating at the third bending mode: (a) shearographic fringe pattern of $\partial w_0/\partial x$, (b) shearographic fringe pattern of $\partial w_0/\partial x$ of the object vibrating at a larger amplitude than that of (a), (c) enhanced fringe pattern of (b).
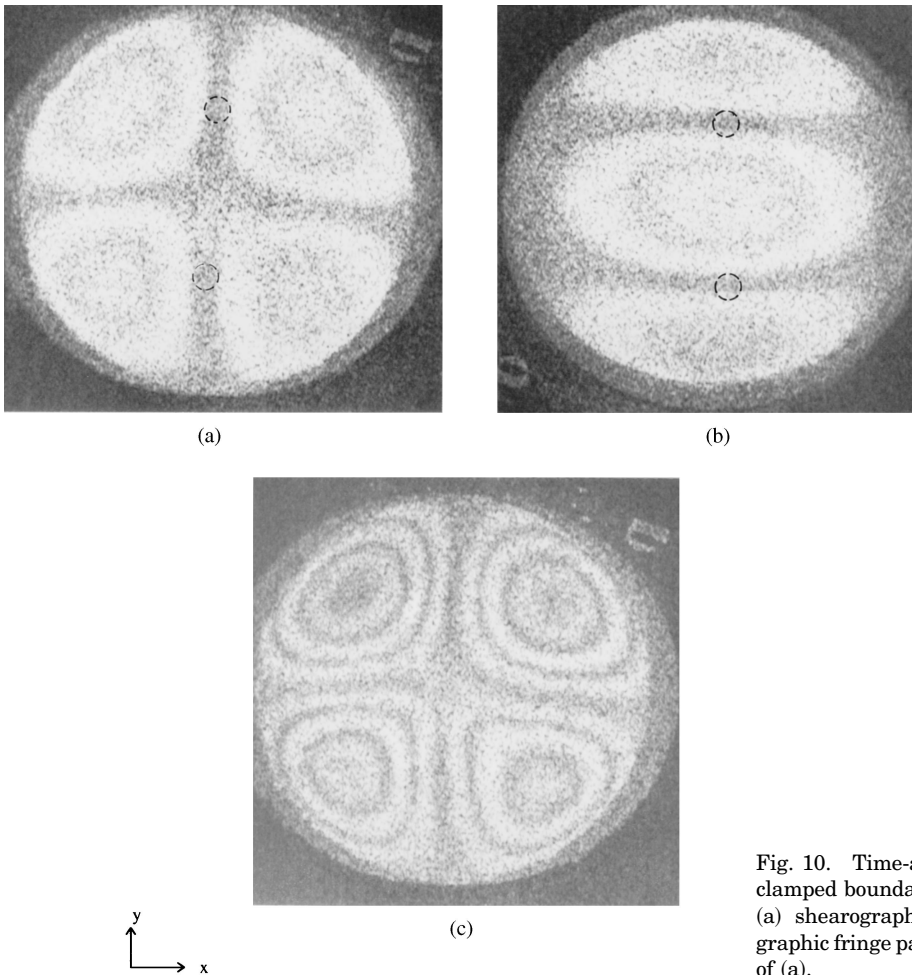
(a)

(b)

(c)

y
x

Fig. 10. Time-averaged fringes of a circular plate with a clamped boundary vibrating at the first asymmetric mode: (a) shearographic fringe pattern of $\partial w_o/\partial x$, (b) shearographic fringe pattern of $\partial w_o/\partial y$, (c) enhanced fringe pattern of (a).

plate. The fringe patterns are experimentally obtained with the time-averaged subtraction method, based on the principle of Eq. (9). The fringe density of the pattern shown in Fig. 9(b) appears to be higher than that shown in Fig. 9(a) because the vibration amplitude for the Fig. 9(b) case is larger. By increasing the excitation force level, we can observe that the fringes appear to be unmoved at the locations numbered by the arrows. The fringes marked with numerals 1 and 3 are the dark fringes corresponding to the zero gradient locations, i.e., antinodal positions. The fringes marked with numerals 2 and 4 have brightness either maxima or minima, corresponding to zero-strain locations, i.e., contraflexural regions. The fringes at these two locations are somewhat obscure. However, when the method of Eq. (12) is used, the fringe contrast is markedly improved, as we can see from Fig. 9(c). In the regions between 1 and 2, 2 and 3, or 3 and 4, fringes appear to be generated from 2 and 4, travel through the in-between regions, and approach 1 and 3 with a denser and denser fringe appearance.

In Figs. 10(a) and 10(b), the fringe patterns are also experimentally generated by the use of the time-averaged subtraction method. Figure 10(a) is optically sheared in the x direction, whereas Fig. 10(b) is sheared in the y direction. The fringe pattern in Fig.

10(a) is quite similar in pattern to that computed (Fig. 5). As we can see in Figs. 10(a) and 10(b), the dark fringe circles can be understood to be caused by the clamped condition along the rim of the plate. They represent the lines of zero gradients, i.e., $\partial w_o/\partial x = 0$ for the former figure and $\partial w_o/\partial y = 0$ for the latter. Away from the clamped rim toward the central regions, the thick crossed lines in Fig. 10(a) represent contours of $\partial w_o/\partial x = 0$. The thick dark elliptic curve in Fig. 10(b) represents the contour of $\partial w_o/\partial y = 0$. Overlapping the two patterns can locate the antinodal position of the vibration mode. The locations are circled as shown in the figures.

To apply the method of Eq. (12), the fringe quality is markedly enhanced for the higher-order fringe loops. As shown in Fig. 10(c), the fringes of the four eyes are clearly visible. These eyes provide a means to trace the elliptic loci of the zero-strain or shear contours as plotted in Figs. 5 and 6. The improvement of the fringe visibility will also facilitate the tracing of such loci in the x as well as in the y directions.

Quite obviously in Fig. 10, the number of fringes in Fig. 10(c) is more than that in Fig. 10(a), although the two patterns represent the same plate vibration level. Similarly, the same is true when comparing Figs. 9(c) with 9(b). This is attributed to the increase in sen-

sitivity with the use of the present frame subtraction method compared with the use of the traditional subtraction method.[3]

5. Conclusion

The principle of a new time-averaged frame subtraction digital shearographic technique for vibration analysis has been described, and experiments have been done for demonstration. The method of subtracting two Bessel fringe patterns at different forcing levels has been found to be capable of enhancing the higher-order Bessel fringes. It facilitates the tracing of the zero-shear-strain and zero-flexural-strain contours. Compared with the phase-shift method, this new frame subtraction method has been found to be more efficient and easier to implement for qualitative vibration measurement. This provides a means for fast inspection of plate vibration behavior.

A fringe interpretation method has been introduced for identifying the antinodal positions and contours of zero strains in beam and plate vibrations, including zero-shear-strain contours in the plate vibration case. A good agreement between theoretical and experimental results has been found in this study.

References

1. K. T. Chan, T. P. Leung, and W. O. Wong, "Free vibration of simply supported beam partially loaded with distributed mass," J. Sound Vib. **191,** 590–597 (1996).
2. O. J. Lokberg, "ESPI—the ultimate holographic tool for vibration analysis?," J. Acoust. Soc. Am. **75,** 1783–1791 (1984).
3. S. Nakadate, T. Yatagai, and H. Saito, "Digital speckle-pattern shearing interferometry," Appl. Opt. **19,** 4241–4246 (1980).
4. K. T. Chan, T. P. Leung, and J. Z. Zhang, "High-speed automatic measurement of out-of-plane displacement using ESPI," Opt. Laser Technol. **25,** 3–8 (1993).
5. A. R. Ganesan, P. Meinlschmidt, and K. D. Hinsch, "Vibration mode separation using comparative electronic speckle pattern interferometry (ESPI)," Opt. Commun. **107,** 28–34 (1994).
6. H. O. Saldner, N. K. Mohan, and N. E. Molin, "Comparative TV holography for vibration analysis," Opt. Eng. **34,** 486–492 (1995).
7. H. Rohleder, P. M. Petersen, and A. Marrakchi, "Quantitative measurement of the vibrational amplitude and phase in photorefractive time-average interferometry: a comparison with electronic speckle pattern interferometry," J. Appl. Phys. **76,** 81–84 (1994).
8. J. A. Leendertz and J. N. Butters, "Image-shearing speckle-pattern interferometer for measuring bending moments," J. Phys. E **6,** 1107–1110 (1973).
9. K. Creath and G. Å. Slettemoen, "Vibration observation techniques for digital speckle-pattern interferometry," J. Opt. Soc. Am. A **2,** 1629–1636 (1985).
10. S. Nakadate, "Vibration measurement using phase-shifting speckle-pattern interferometry," Appl. Opt. **25,** 4162–4167 (1986).
11. S. L. Toh, H. M. Shang, F. S. Chau, and C. J. Tay, "Flaw detection in composites using time-average shearography," Opt. Laser Technol. **23,** 25–30 (1991).
12. Y. Y. Hung, "Shearography: a new optical method for strain measurement and nondestructive testing," Opt. Eng. **21,** 391–395 (1982).
13. J. W. Goodman, "Statistical properties of laser speckle patterns," in *Laser Speckle and Related Phenomena*, J. C. Dainty, ed. (Springer-Verlag, Berlin, 1975), Vol. 9, pp. 9–75.
14. G. Chen and J. X. Zhou, *Vibration and Damping in Distributed Systems* (CRC Press, Boca Raton, Fla., 1993).